

Emergence of reentrant structural modulations far beyond the thermal limit

Nitish Mathur¹, Guangming Cheng², Francesc Ballester^{3,4}, Gabrielle Carrel¹, Vincent M. Plisson⁵, Fang Yuan¹, Jiangchang Zheng⁶, Caiyun Chen⁶, Scott B. Lee¹, Ratnadwip Singha^{1,7}, Sudipta Chatterjee¹, Kenneth S. Burch⁵, Berthold Jäck⁶, Ion Errea^{3,4,8}, Maia G. Vergniory^{3,9}, Nan Yao², Leslie M. Schoop^{1*}

1. Department of Chemistry, Princeton University, Princeton, NJ 08544, USA.
2. Princeton Materials Institute, Princeton, NJ 08544, USA.
3. Donostia International Physics Center, 20018 Donostia-San Sebastián, Spain.
4. Department of Applied Physics, University of the Basque Country (UPV/EHU), 20018 Donostia-San Sebastián, Spain.
5. Department of Physics, Boston College, Chestnut Hill, MA USA.
6. Department of Physics, The Hong Kong University of Science and Technology, Clear Water Bay, Kowloon, Hong Kong SAR.
7. Department of Physics, Indian Institute of Technology Guwahati, Assam 781039, India.
8. Centro de Física de Materiales (CSIC-UPV/EHU), 20018 Donostia-San Sebastian, Spain.
9. Département de Physique et Institut Quantique, Université de Sherbrooke, Sherbrooke, J1K 2R1 Québec, Canada.

Corresponding author* (email): lschoop@princeton.edu

ABSTRACT: A single material can exist in different states, with solids, liquids, and gases being the most familiar examples. In materials, these states can exhibit periodic structures spanning from atomic to macroscopic length scales. The conventional wisdom is that a low-symmetry periodic structure transitions into a high-symmetry structure as temperature increases beyond the critical point, which is defined by a thermal limit. In this work, we demonstrate an unforeseen emergence of low-symmetry modulated structures with a reentrant phase in nanoflakes of two-dimensional TaCo₂Te₂ far beyond their thermal limit, using in-situ heating transmission electron microscopy. We contend that entropy can drive the reappearance of structural modulations, consistent with predicted dynamic structural instabilities in undistorted TaCo₂Te₂, and further supported by Raman measurements. These findings not only reveal unexpected phase transitions in a crystalline material but also present a new pathway for creating novel ordered phases in low-dimensional systems.

Main text

Modulated structures represent a distinct class of materials where atomic positions systematically deviate from the ideal periodic lattice in one or more crystallographic directions^{1,2}. Crystals adopt these low-symmetry modulated structures with long-range order (LRO) due to energetically favorable interactions between electronic³, orbital⁴, or magnetic states⁵ and the underlying lattice. Such modulations enable fine-tuning of material properties through directional control, offering tailored functionalities and material-design strategies⁶. At temperatures above the critical point (T_c), the low-symmetry modulated structure transforms into a high-symmetry unmodulated structure. This transition becomes energetically favorable as increased entropy overcomes interactions driving structural modulations. It marks the conventional thermal limit of modulated structures, beyond which the high-symmetry structure exhibits classical behavior as the temperature rises. It is unknown whether the LRO in modulated structures can reemerge above T_c , which seems counterintuitive as entropy usually favors disorder.

Entropy can drive LRO under special conditions^{7,8}. An entropy-stabilized ordered phase can paradoxically increase the system's overall entropy by generating more configurations than the random movements in a disordered state. This non-classical phenomenon generally governs order *via* self-assembly mostly studied in colloidal mixtures^{9,10}, soft matter^{11,12}, and biological systems¹³. In these systems, greater conformational flexibility and pronounced thermal fluctuations effects can promote entropic-stabilization of ordered phases, which are more difficult to achieve in crystalline solids. The concept of entropic stabilization of ordered phases in purely crystalline materials¹⁴, though not entirely unknown, is rarely seen. Modulated structures can offer more structural flexibility compared to a typical crystalline solid, thus they can be the perfect testbed to study if entropy can disfavor the high-symmetry structure above T_c and hence drive a reemergence of a low-symmetry modulated structure. To the best of our knowledge this phenomenon has not yet been observed in a structurally modulated material.

In this work, we demonstrate the reemergence of LRO above T_c in thin flakes of the layered van der Waals (vdW) material TaCo₂Te₂, which exhibits structural modulations known as Peierls distortion. Using in-situ heating within a transmission electron microscope (TEM), we observe the emergence of low-symmetry structure with multiple LROs and a reentrant phase above T_c . First-principles calculations unveil a high phonon entropy associated with dynamic structural

instabilities in undistorted TaCo₂Te₂. We propose that entropy-stabilization could be responsible for the reemergence of structural modulations in TaCo₂Te₂ thin samples, even in the presence of enhanced thermal fluctuations and expected material inhomogeneities. This unprecedented regime of LRO in structurally modulated TaCo₂Te₂ offers a new perspective on phase transformations in crystalline solids, suggesting such phenomenon may be less rare than previously thought.

Structural modulations in TaCo₂Te₂

TaCo₂Te₂ is a metallic vdW material with an orthorhombic structure (space group *Pnma*) and a sextuple-atomic-monolayer^{15, 16}. TaCo₂Te₂ exhibits a Peierls distortion along the crystallographic *a*-axis at room temperature (RT) (**Fig. 1a**). To obtain a high-symmetry undistorted TaCo₂Te₂ structure (**Fig. 1b**), where the unit-cell is halved along the *a*-axis, the system must be heated above RT. This undistorted structure is isostructural with TaNi₂Te₂ (see Supplementary Fig. 1). Notably, both the distorted and undistorted structures of TaCo₂Te₂ exhibit metallic bands in their respective calculated electronic band structures (Supplementary Fig. 2). Using chemical vapor transport (CVT), we synthesized single crystals of TaCo₂Te₂ (see Methods, Supplementary Fig. 3 and Supplementary Table1). We found that mechanically exfoliated TaCo₂Te₂ nanoflakes exhibit good air-stability and can be easily exfoliated to a few layers from bulk crystals (Supplementary Fig. 4). TEM samples were prepared both by transferring exfoliated nanoflakes onto a TEM grid and by cutting a single crystal with a focused ion beam (FIB). Cross-sectional scanning transmission electron microscopy (STEM) images (**Figs. 1c,d** and Supplementary Fig. 5) elucidate the transition from the RT distorted structure to the undistorted high temperature structure as illustrated in **Figs. 1a,b**. All selected area electron diffraction (SAED) images collected in our study are indexed relative to the RT distorted phase. The main reflections of TaCo₂Te₂ RT phase also constitute peaks (q_c) corresponding to the distorted unit cell shown in the SAED image of *ab*-plane (**Fig. 1e**). In addition, we observe forbidden reflections of space group *Pnma* ($h, k = 2n-1$ or 0 ; $h \neq k$; n is an integer), and a slight deviation of the angle between a^* and b^* (Supplementary Fig. 6). This can be attributed to monoclinic distortions arising from sliding between and within layers, often caused by residual strains during nanoflake preparation.^{17, 18}

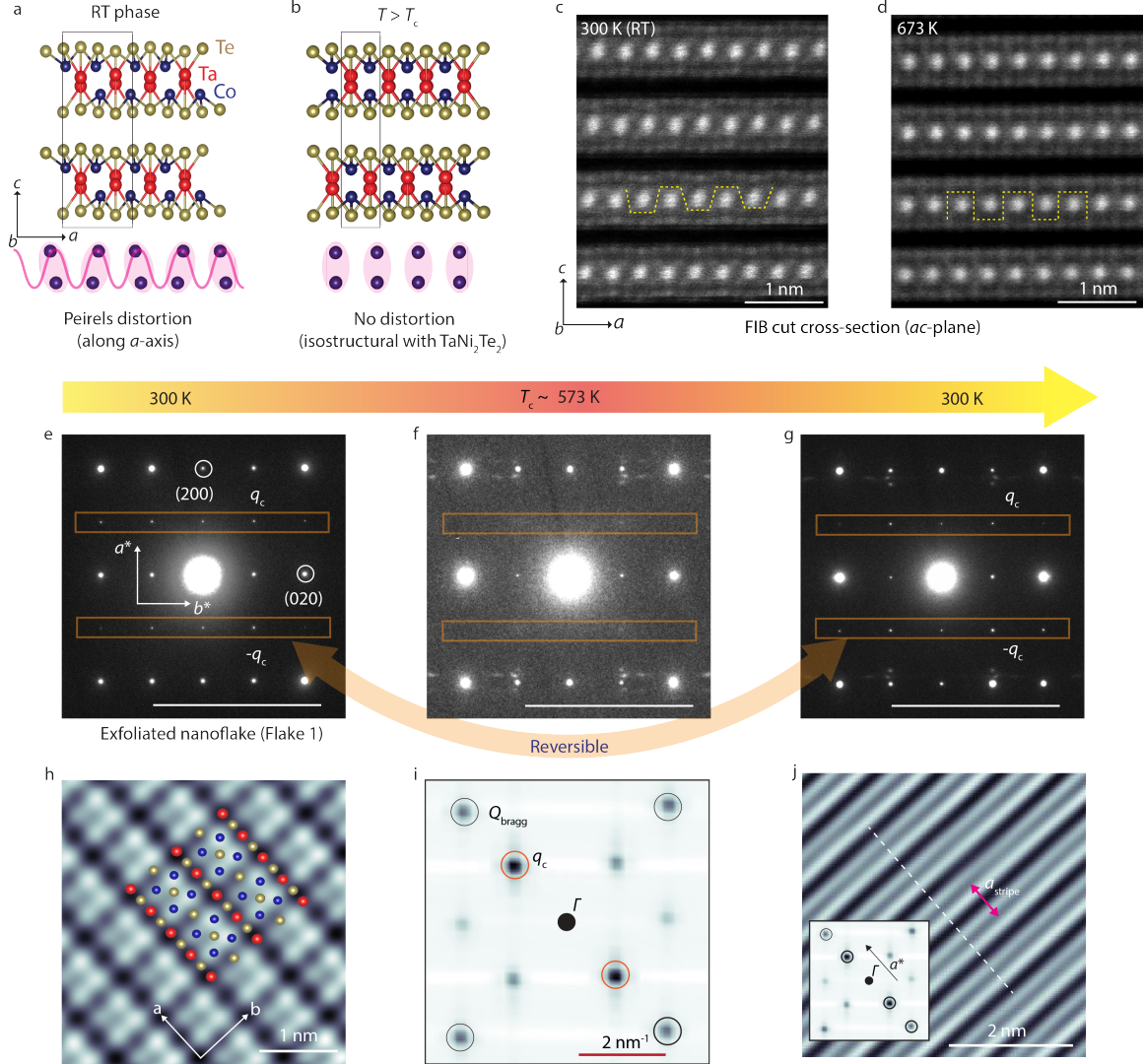


Fig. 1: Structural modulations in TaCo₂Te₂ (a) Crystal structure of the room temperature (RT) phase of TaCo₂Te₂ with a Peierls distortion along the crystallographic *a*-axis and (b) crystal structure of the undistorted phase above T_c . Black boxes represent unit cells of both phases (c,d) Cross-sectional STEM images of *ac*-plane showing the transformation from the RT distorted structure to the undistorted structure. Dotted yellow lines highlight Co atomic chains matching with corresponding crystal structures in panel a,b (e-g) SAED images revealing T_c and reversible structural transition in an exfoliated TaCo₂Te₂ nanoflake (Flake 1). Diffraction peaks associated with the Peierls distortion, marked with orange boxes, reveal the presence and absence of commensurate wave-vector ($\pm q_c$) when compared with the lattice parameter of the undistorted reciprocal unit cell, a^*_{200} . (h) High-resolution STM topographic image of TaCo₂Te₂ (taken at $T \sim 4.2$ K) with the atomic structure of the sextuple-monolayer superimposed. (i) FFT of the STM image in panel h, where Bragg and modulation peaks marked with black and orange circles, respectively (j) The real space pattern obtained by performing an inverse FFT on peaks along the a^* direction as shown in the FFT inset image. Intensity profile of the stripe-like pattern was collected along the dashed white line. The real-space modulation vector is a_{stripe} . Scale bar in panels e-g is 5 nm^{-1} . All SAED and reciprocal space images are indexed with respect to the RT distorted structure.

The temperature-dependent structural evolution of the distorted phase exhibits incoherent peaks at q_c when the temperature reaches $T_c \approx 573$ K. At this point, the structure losing its low-symmetry distorted phase and transitions to a high-symmetry undistorted state. (Fig. 1f). Furthermore, the distorted structure can be fully recovered after cooling down from T_c (Fig. 1g),

demonstrating a reversible structural transition. The distorted structure has a commensurate wave vector, where $q_c \approx a^*_{200}/2$ and a^*_{200} is the lattice parameter of the undistorted reciprocal unit-cell (Supplementary Fig. 6f). Scanning tunneling microscopy (STM) topography conducted at ~ 4.2 K shows the atomically resolved lattice of the TaCo₂Te₂ (001) surface (**Fig. 1h**). Fourier transformed (FFT) image of the topography reveal modulation peaks in addition to Bragg peaks like the SAED image at RT (**Fig. 1i**). We determine the corresponding real space modulation ($a_{\text{stripe}} \approx 0.67 \pm 0.01$ nm) from the stripe-like pattern by performing an inverse FFT on peaks along a^* direction (**Fig. 1j** and Supplementary Fig. 7). This value is close to the RT lattice parameter ($a = 0.66$ nm) of TaCo₂Te₂ distorted structure. Both TEM diffraction and STM images show that the Peierls distortion in TaCo₂Te₂ is stable over a wide range of temperatures (4 – 573 K). Henceforth, we will refer to the RT distorted structure of TaCo₂Te₂ as the primary order.

Persistence of short-range order and the reemergence of LRO above T_c

In-situ heating of an exfoliated TaCo₂Te₂ nanoflake above T_c (**Fig. 2a**) within the TEM leads to the incoherence of the primary order. The selected area electron diffraction (SAED) image captured at 593 K ($> T_c$) reveals diffuse scattering peaks at q_c , indicating the persistence of short-range order (SRO) (**Fig. 2b**). The SRO is a partially melted state of the primary order. Surprisingly, we observe the reemergence of LRO by continuously increasing temperature above T_c , which manifests as one-dimensional (1D) superlattice peaks along the a^* direction and more clearly visible in the SAED image collected at 723 K (**Fig. 2c**). After allowing the sample to cool and rest at RT for approximately 15 hours, the presence of superlattice peaks in the SAED image indicate an irreversible phase transition (**Fig. 2d**). We compare the representative superlattice peaks along the a^* direction for both ($h30$) and ($h40$) planes shown in SAED images (**Figs. 2e,f**) collected at 723 K and RT (post-cooled). This analysis reveals commensurate wave-vectors of $q_n \approx (a^*_{200}/2) \times (1/n)$, with $n = 2$ and 4 (**Fig. 2g**). Furthermore, we observe the emergence of two incommensurate wave-vectors, ($q_{1,2}$ (IC)) $\approx 0.70a^*_{200}$ and $0.41a^*_{200}$, along ($h30$) and ($h40$) planes, respectively. It is possible that the relationship between $q_{1,2}$ (IC) can be expressed as $2q_1$ (IC) $- 1 = q_2$ (IC). The interplanar spacing of underlying undistorted lattice does not significant change along the a^* direction above T_c (Supplementary Fig. 8). We further exclude the presence of a high-temperature polymorph of TaCo₂Te₂ by single-crystal X-ray and TEM diffraction measurements of TaCo₂Te₂ crystals quenched from 773 K (Supplementary Fig. 9).

As the temperature rises above T_c , the SRO diffuse peaks still maintain the periodicity of low-symmetry distorted phase which differs from the periodicity of the underlying undistorted

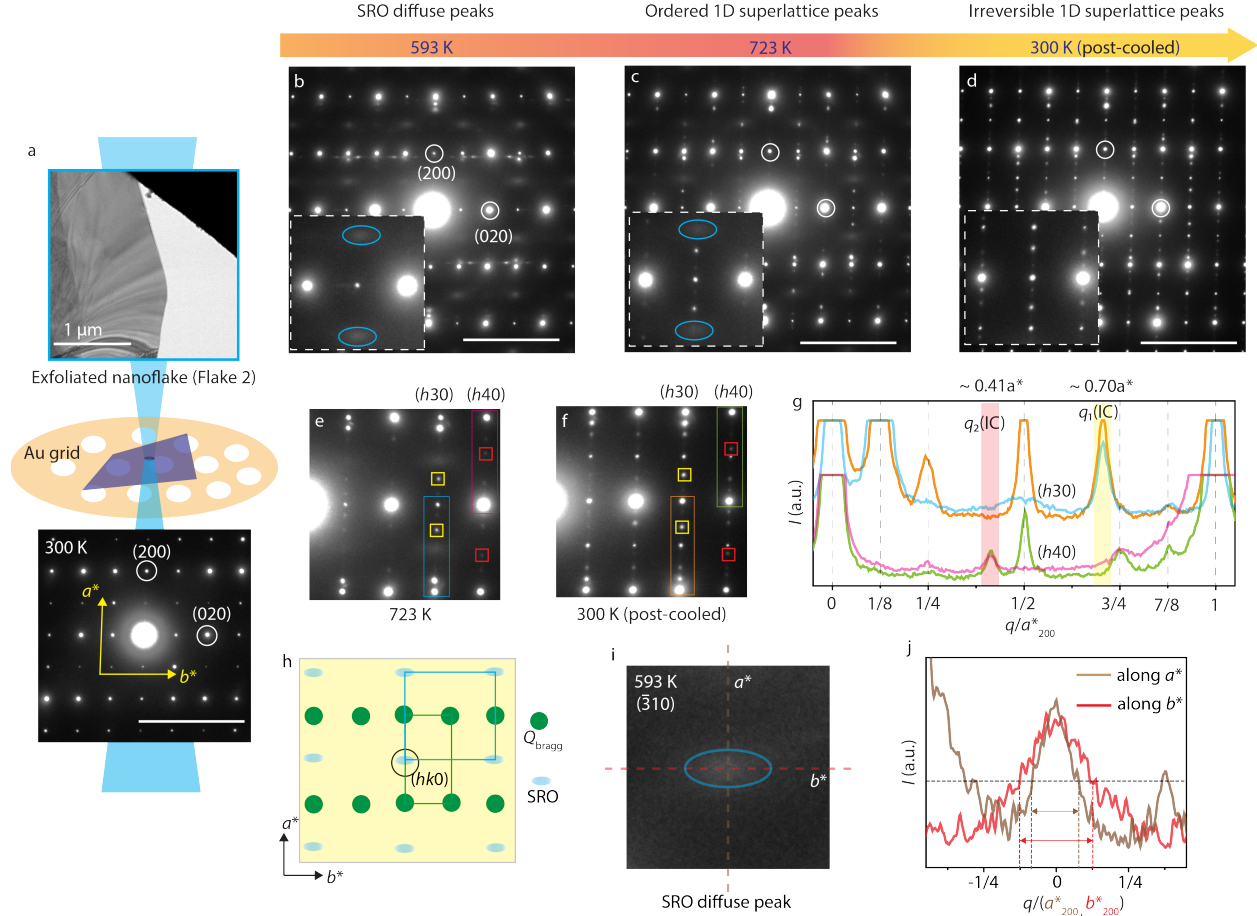


Fig. 2: Reemergence of LRO above T_c in TaCo_2Te_2 thin flakes: (a) Schematic depicting the experimental setup for collecting SAED images on an exfoliated TaCo_2Te_2 nanoflake (Flake 2) transferred to a Au TEM grid. (b-d) Temperature evolution of undistorted TaCo_2Te_2 structure shown in SAED images above T_c . Insets highlighting SRO diffuse peaks, marked by blue ellipsoids, accompanied by sharp superlattice peaks from symmetry breaking LROs, which can be irreversibly cooled back to RT. (e,f) Zoomed images of SAED patterns at 723 K and RT (post-cooled). (g) Representative intensity line scans along the a^* direction for $(h30)$ and $(h40)$ planes in reciprocal space, as shown in panels e and f. The colors of rectangular boxes marked in panels e and f correspond to the colors of trace lines in the intensity plot. Yellow and red colored boxes marked the $q_1(\text{IC})$ and $q_2(\text{IC})$ peaks, respectively. (h) Schematic depicting the comparison between the arrangement of SRO diffuse peaks and underlying crystal lattice above T_c in reciprocal space. (i) Intensity spread of a representative diffuse SRO peak in reciprocal space. (j) Intensity line scan of the diffuse SRO peak, obtained along a^* and b^* directions shown in panel i. Correlation length is determined at FWHM intensity. Scale bar in panels a-d is 5 nm^{-1} .

TaCo_2Te_2 lattice (**Fig. 2h**). We determine the preferred orientation of incoherent structural domains above T_c by measuring the spread of a representative SRO diffuse peak at the full-width half maximum (FWHM) intensity along the a^* and b^* directions (**Figs. 2i,j**). The SRO correlation length is longer along the a -axis ($\approx 2.12 \text{ nm}$) compared to the b -axis ($\approx 1.35 \text{ nm}$). This preferred alignment of incoherent structural domains implies a greater reduction in the configurational

entropy along the a -axis compared to the b -axis. It is important to note that TEM measurements provide structural information averaged over a sub-micron flake area. Hence, the influence of sample inhomogeneities on the observed phenomenon is effectively captured in TEM images¹⁸,¹⁹. It might cause some minor deviations of superlattice peaks within different samples as detailed in the Supplementary Table 2. Nevertheless, the reemergence of low symmetry modulated structure above T_c is consistently observed across different samples, with these new LROs characterized by similar wave vectors. (Supplementary Fig. 10).

Emergence of reentrant primary order

We next conduct in-situ heating TEM experiments on an in-plane FIB cut lamella (**Fig. 3a**), a method distinctly different from the previously studied exfoliated/transferred TaCo₂Te₂

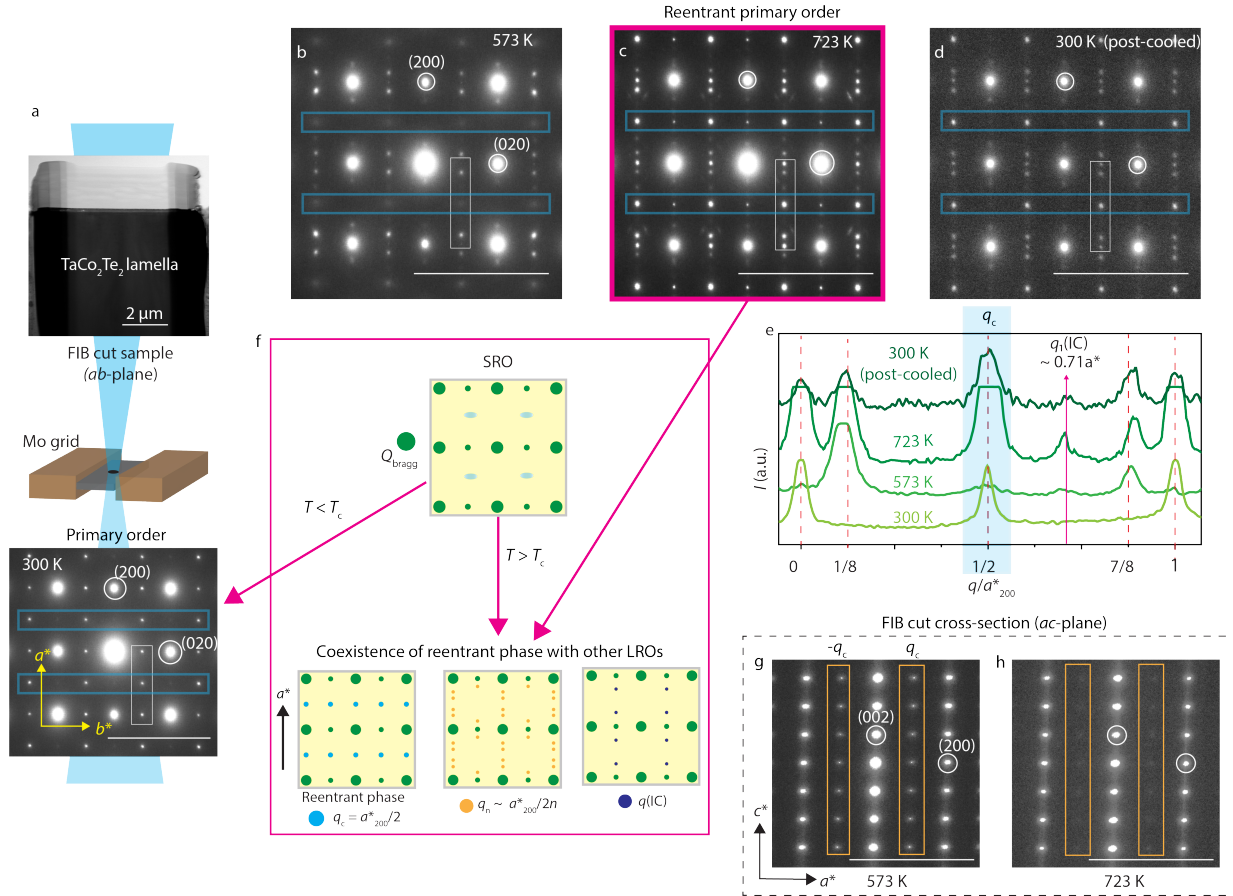


Fig. 3: Emergence and coexistence of reentrant phase far above T_c : (a) Schematic depicting the experimental setup for collecting SAED images on a FIB cut TaCo₂Te₂ lamella (ab -plane) attached to a Mo grid. (b-d) Temperature evolution of the undistorted TaCo₂Te₂ structure above T_c shown in SAED images. (e) Representative intensity line scans of SAED peaks marked with white boxes along the a^* direction in panels a-d. Temperature evolution of the primary order peaks (q_c) marked with blue colored box, highlighting the emergence of the reentrant phase at 723 K far above T_c . (f) Schematic showing the reemergence and coexistence of LROs and the reentrant phase above T_c starting from the partially melted primary order. SAED images of FIB cut cross-section of ac -plane collected at (g) 573 K and (h) 723 K. Orange boxes highlight weak q_c peaks at 573 K, which almost disappear at 723 K. Scale bar in panels a-d and g,h is 5 nm^{-1} .

nanoflakes to verify the robustness of reemerging LRO in TaCo₂Te₂. Indeed, acquired SAED images (**Figs. 3b-d**) with increasing temperature above T_c show reemerging LROs with similar wave-vectors (q_n (where $n = 2, 4$) and $q(\text{IC}) \sim 0.70 a^*_{200}$) just as in exfoliated nanoflakes. Remarkably, we observe the reemergence of sharp q_c peaks from diffuse SRO peaks at 723 K, indicating the reentry of the primary order (**Fig. 3e**), which is also evident in other exfoliated flake samples (Supplementary Fig. 10). While reentrant phases have been observed in other modulated structures such as charge density wave materials, achieving this reentry typically requires the application of high external pressures in the gigapascal range^{20, 21}. Here, the reentrant primary order appears just with increasing temperature. Notably, the reentry of the primary order does not diminish the coherency of other LROs (q_n and $q(\text{IC})$). This coexistence seems to play a key role in the uncanny stabilization of the reentrant primary order (**Fig. 3f**). However, we examined a TaCo₂Te₂ cross-sectional TEM sample (ac plane) and observed no reemergence of LRO along the a^* direction up to 723 K (**Figs. 3g,h**). Hence, the thin ab -plane samples of TaCo₂Te₂ appear to favor low-symmetry LROs phase over a high-symmetry undistorted phase above T_c .

Before the emergence of LRO and the reentrant phase in TaCo₂Te₂ nanoflakes above T_c , we also observe weakly coherent peaks, manifesting as diffuse streaks in SAED images, emerging in multiple directions in reciprocal space (**Figs. 1f,g** and Supplementary Fig. 11). To determine whether these weakly ordered peaks are associated to lattice strain caused by thermal expansion at high temperatures, we heat the flakes near the temperature where streaks typically appear in SAED images ($T_c \approx 573$ K), and then cool the system back to 300 K. Like superlattice peaks from LRO, these weakly coherent peaks also exhibit irreversible phases, as demonstrated in the zoomed SAED image near a Bragg peak in **Fig. 4a** (see Supplementary Fig. 10 for enlarged images). However, unlike LRO superlattice peaks, which intensify with increasing temperature, these weak peaks gradually disappear as the temperature rises (**Figs. 4b-d**). This temperature-dependent behavior suggests that increasing thermal fluctuations favors stable anisotropic LRO along the a^* direction but disrupts coherency of ordered phases in all other directions. We further demonstrate the effect of continuous heating on coherency of reentrant peaks by collecting time-dependent SAED images at 723 K, where the reentrant phase emerges (**Figs. 4e,f**). We observe that the intensity of reentrant peaks enhanced when maintaining this temperature for approximately 240 minutes (see other example in Supplementary Fig. 12). This suggests that the emergence of LROs increases the overall entropy of the system more than the partially melted SRO state in the in-plane geometry

(*ab*-plane) of TaCo₂Te₂ nanoflakes. **Fig. 4g** shows a schematic of a temperature *vs* disorder phase diagram to compare observed phenomenon in our study with conventional classical models. Our observations challenge conventional models where increasing thermal fluctuations and material defects (such as vacancies and quenched disorder) should disrupt the LRO coherence above T_c^{22} ,

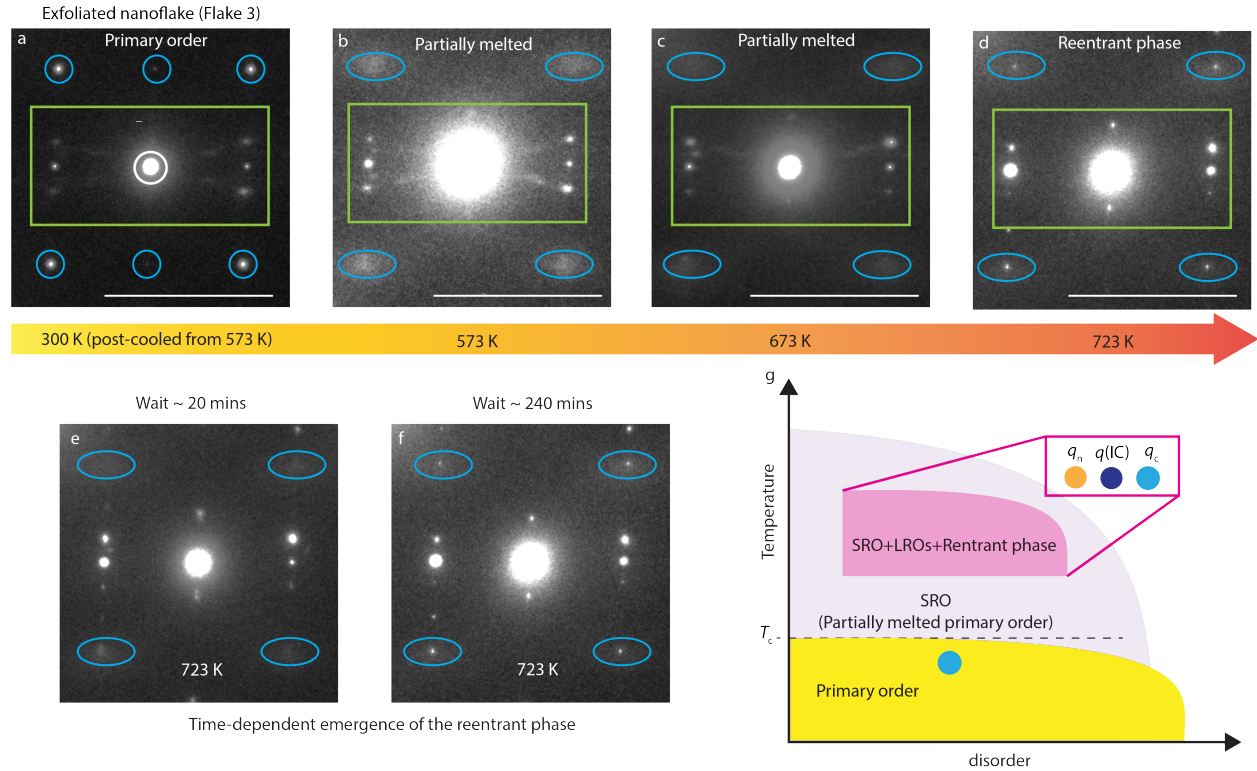


Fig. 4: Temperature and time-dependent emergence of anisotropic LROs and the reentrant phase. (a-d) Zoomed SAED images near a Bragg peak collected on an exfoliated nanoflake (Flake 3), exhibiting the temperature evolution of anisotropic LRO along a^* direction and disappearance of weakly ordered peaks in multiple directions in reciprocal lattice. Blue circles and ellipsoids highlight peaks of the primary order and SRO/reentrant phase, respectively. Green boxes highlight the weakly coherent peaks along multiple directions in reciprocal space (e,f) Time-dependent emergence of the reentrant phase at 723 K. (g) Schematic of temperature *vs* disorder phase diagram depicting the transition from partially melted primary order to anisotropic LROs and the reentrant phase above T_c in TaCo₂Te₂ nanoflakes.

^{23, 24}. We observe the stabilization of low symmetry modulated phases which transition from a partially melted state above T_c . This process involves the formation of weakly coherent intermediate phases before reaching anisotropic LROs and the reentrant phase.

Structural instabilities of undistorted TaCo₂Te₂

TEM observations show significant lattice distortions and the reemergence of multiple LROs, indicating the presence of structural instabilities above T_c . Phonon-dispersion calculations for the undistorted structure of TaCo₂Te₂ reveal pronounced imaginary frequencies across multiple high-symmetry Brillouin zone points (Figs. 5a,b)²⁵. This points to the observed dynamic structural instabilities, which suggests a high phonon entropy in the undistorted TaCo₂Te₂ (Supplementary

Fig. 13). While the phonon-bands calculations were conducted without incorporating the thermal contributions, we carried out Raman measurements (Fig. 5c) on an exfoliated TaCo₂Te₂ nanoflake (Supplementary Fig. 14) within a glovebox²⁶ at various temperatures to determine changes in collective phonon modes above T_c . We show Raman spectra from RT up to 600 K, with each temperature offset for better visibility. The RT spectrum consists of a cluster of 5 modes from 87 cm⁻¹ to 165 cm⁻¹ with 2 more weak modes from between 250 cm⁻¹ and 300 cm⁻¹. There are two particularly interesting aspects of the temperature dependent results that we focus on; the sudden change in the spectrum near T_c and the evolution of the P3 and P5 modes over the whole

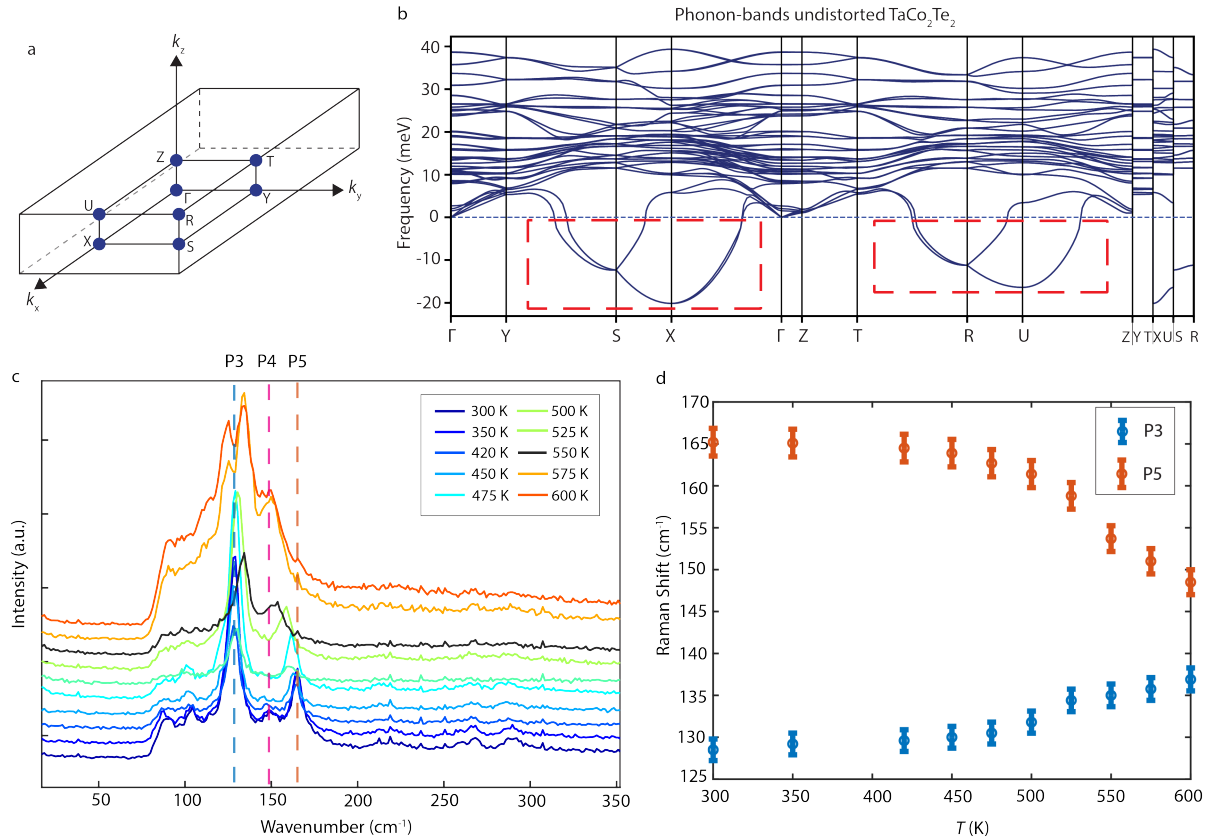


Fig. 5 : Structural instabilities of undistorted TaCo₂Te₂ above T_c . (a) 3D Brillouin zone of the undistorted TaCo₂Te₂ structure used for first principle calculations. (b) Phonon band calculations of the undistorted TaCo₂Te₂ above T_c . Dashed red boxes highlight imaginary phonon bands expand over a wide region of the Brillouin zone. (c) Raman spectrum collected on a TaCo₂Te₂ nanoflake at various temperatures above RT. Raman modes P3, P4, and P5 marked with blue, pink, and orange dashed lines, respectively. (d) Corresponding temperature dependence of P3 and P5 Raman peak shifts.

temperature range. While the spectra evolve continuously with increasing temperature, we see a significant change in the overall spectrum around 550 K with the appearance of a double peak near the P3 mode at 135 cm⁻¹. At the same time, the weak P4 mode appears to vanish. These two features become even more significant at the highest temperatures above T_c . Beyond the differences in the

overall spectra above and below T_c , our measurements also reveal an unusual shift in Raman peaks of the P3 mode and extreme broadening of the P5 mode with increasing temperature, indicative of strong phonon softening above T_c . The energy shifts of both these modes are plotted in **Fig. 5d**. Typically, phonons shift to lower energies with increasing temperatures as the lattice expands. This is exactly the behavior of the P5 mode. The P3 mode however shifts to higher energy with increasing temperature. This behavior is indicative of additional higher order anharmonic terms²⁷, most likely due to some avoided band crossing or structural transition and could be reflective of the onset of LRO above T_c .

Discussion

We unambiguously showed the reemergence of LROs and the reentrant primary order in a two-dimensional TaCo₂Te₂ above T_c . This raises the main question – how the presence of ordered modulated phases above T_c increases the overall entropy to minimize the free energy of the system. Here, we provide a qualitative analysis of this complex entropy-driven stabilization of LROs at high temperatures in TaCo₂Te₂ where significant effects of thermal fluctuations and material inhomogeneity are expected. In the undistorted TaCo₂Te₂ structure, predicted dynamic structural instabilities indicate high phonon entropy within the system. While these structural instabilities expand over a wide region in the Brillouin zone, we observe preferential orientation of LROs specifically along the a^* direction. This preferential anisotropic order may increase the system's overall entropy compared to a scenario where weakly coherent orders emerge in multiple directions due to inherent structural instabilities. This shares characteristics with non-classical nucleation and growth processes in materials where multiple sequential intermediates form to achieve highly anisotropic or hierarchical phases²⁸.

The emergence of LROs along the a^* direction doesn't necessarily lead to a decrease in configurational entropy. We compare this to the SRO lattice, as a completely disordered state is never observed above T_c in our TEM experiments. The persistence of the SRO state far above the T_c is indicative of remnant incoherent domains of the primary order that can pin to thermally induced vacancies and quenched disorders^{29, 30}. These pinning effects could further increase with the temperature and reduce the entropy of the SRO lattice. On the other hand, LRO could form in a low-disorder region of TaCo₂Te₂ thin flakes above T_c . Previous studies on 1T-TaS₂ endotaxial heterostructures show that the low-disorder regime is essential for the emergence of hidden CDW

phases at high temperatures^{18, 31, 32}. These reemerging structurally modulated phases in a low disorder regime could be more receptive to thermal fluctuations along the a^* direction, which should be enhanced in a low-dimensional system like TaCo_2Te_2 ³³. This could offer higher entropy-stabilization of the LRO states compared to the pinned SRO.

In thin in-plane TEM samples of TaCo_2Te_2 , we observed mesoscopic defects such as nanoflake folds, wrinkles, and microcracks, which generally induce differential stress. These mesoscopic defects can create local strain gradients across the nanoflake. Additionally, thermally induced vacancies and quenched disorders increase the energy barrier for stress relaxation, enabling strain gradients even at high temperatures. Strain gradients can modify lattice vibrational modes - compressive strain typically stiffening phonon modes and tensile strain softening them^{34, 35}. This can directly influence possible structural configurations of the SRO state which can either assist or restrict the emergence of LROs above T_c ³⁶. Although similar defects and thermal fluctuations can exist in a cross-sectionally prepared sample, the presence of free edges in thin in-plane areas ($\approx 50\text{-}100$ nm) provides effective pathways for strain relaxation to reduce in-plane strain gradients, contrary to exfoliated nanoflakes. Strain gradients in thin samples appear to modify the energy landscape, creating kinetic traps for the reemerged LRO states and may explain the irreversibility of these high-temperature phases. In this scenario, these states become trapped in metastable valleys within the energy landscape, making complete phase reversal by disrupting the LRO increasingly unlikely with decreasing temperature. The origin of the reentrant primary order and other LRO states could stem from either phonon-phonon or electron-phonon coupling in this material. However, this mechanism remains unclear and requires further investigation.

While these arguments do not fully explain the complex mechanism behind the reentrant structural modulations in TaCo_2Te_2 , they offer an intuitive understanding of this dynamic process above T_c . Using in-situ heating within a TEM, we observe a hidden regime of the ordered state that cannot be fully explained by classical phase transformation models. We show accessibility of reemergent LROs at RT, which would be advantageous for designing future experiments involving optical, strain, and electrical perturbations to probe the unexplored dynamics of this new LRO regime. Our work motivates the development of new theoretical frameworks to provide a microscopic understanding of this complex ordering mechanism above T_c and to classify its unique characteristics, particularly in crystalline materials.

Methods

Single crystal synthesis and characterization of TaCo₂Te₂: Bulk single crystals of TaCo₂Te₂ have been synthesized using chemical vapor transport (CVT). Synthesis of large single crystals of TaCo₂Te₂ was adopted from ref ¹⁶. Oriented single crystals with long axis along the *a*-direction prepared from elemental powder of Ta (Sigma-Aldrich 99.99%), Co (Sigma-Aldrich 99.9%) and Te (Sigma-Aldrich 99.999%), mixed in stoichiometric amount with 30 mg iodine chunks (Sigma-Aldrich 99.9%) and sealed in an evacuated quartz tube, which was heated to 1273 K for 10 days in a box furnace. Acquired mm-sized oriented TaCo₂Te₂ single crystals picked from the post-reaction powder mixture using an optical microscope. Quenched single crystal samples were prepared as follows: Post-reaction TaCo₂Te₂ crystals were sealed in an evacuated quartz tube and heated in a box furnace. The temperature was raised to 773 K at a rate of 150 K/hr and maintained for 2 hours before quenching. The morphology and elemental composition of grown crystals were determined using Quanta 200 FEG ESEM equipped with energy dispersive X-ray (EDX) operating at 15 kV. Single-crystal X-ray diffraction (XRD) measurements were conducted on single crystals size < 100 μm using a Bruker D8 VENTURE diffractometer with a PHOTON III CPAD detector and a graphite-monochromated Mo-*K*_α radiation source. All structure refinements were performed using the OLEX2 software package.

TaCo₂Te₂ nanoflake preparation: TaCo₂Te₂ single crystals were mechanically exfoliated using Scotch Magic tape (3M). Prior to the transfer process, SiO₂/Si substrates with a 285 nm oxide layer were thoroughly cleaned by ultra-sonication with acetone, followed by the removal of organic residues using Ar/O₂ (45/15 sccm) plasma cleaning (PE-50 PLASMA ETCH INC) for approximately 5 minutes. Following the preparation of the substrate, large density of lateral micron-sized vdW thin nanoflakes, with varying thicknesses, were transferred to the cleaned Si substrate. Atomic force microscopy (Bruker Dimension Icon AFM) was performed on thin exfoliated nanoflakes, and images were processed using NanoScope Analysis software. These flakes were picked up in ambient conditions from the Si substrate using polymer stamps and transfer stage equipped with micro-manipulators. Glass-slide stamps were prepared using polycaprolactone (PCL, Sigma Aldrich, M_n: 80000) solution (10% weight in chloroform) spin-coated onto the dome-shaped PDMS. Initially, a TEM Au grid (G2000HAG, Ted Pella INC.) was attached to a bare Si/SiO₂ substrate using polycarbonyl (PC) solution. Multiple nanoflakes were

then picked up and transferred onto the grid/Si substrate following the process detailed in ref.³⁷. Subsequently, the entire grid/Si substrate assembly was immersed in a chloroform solution for 20 mins to dissolve the post-transfer PC and PCL polymers. Finally, the TEM grid was carefully scooped from the chloroform solution and air-dried for 1 min.

FIB fabricated thin lamella: TEM thin lamellae were prepared using focused ion beam (FIB) cutting with a FEI Helios NanoLab™ 600 dual beam system (FIB/SEM). Oriented single crystals of TaCo₂Te₂, with their long axis along the *a*- direction, were used as a guide to fabricate multiple lamellae for TEM measurements. These lamellae were cut both in-plane (*ab*-plane) and cross-sectionally (*ac*-planes) using FIB techniques. FIB lamella was attached to Mo grid (10GM02, Ted Pella PELCO®) *via* in-situ Pt deposition at shared edges.

TEM microscopy: In-situ heating TEM experiments were conducted using a Gatan double-tilt holder (Model 652) within the TEM column with base pressure $\approx 10^{-7}$ torr. Temperatures were set and monitored using a Gatan temperature controller (1905). After reaching the set temperature, the electron beam was blanked, and the sample was allowed to equilibrate for approximately 20 minutes to minimize thermal drift before starting image collection. In-situ cooling was achieved by setting 300 K (27 °C) on the controller and waiting overnight (~ 15 hrs) before acquiring images. Selected area electron diffraction (SAED) and atomic resolution HAADF images were collected on a double Cs-corrected FEI Titan Cubed Themis 300 scanning/transmission Electron Microscope (S/TEM). The high-resolution STEM (HRSTEM) images were processed using the Gatan Microscopy Suite software. The electron diffraction simulations were performed using the CrystalMaker and SingleCrystal software package. Crystal structures schematics of TaCo₂Te₂ prepared using VESTA 3 software. ImageJ software was used for determining intensity line scans of diffraction peaks in SAED images.

Glovebox Raman measurements: Air-stability of TaCo₂Te₂ exfoliated nanoflakes was determined using Argon glovebox Raman setup²⁶. Nanoflakes were first exfoliated onto a Si substrate within the glovebox environment. Raman spectra were collected immediately after exfoliation inside glovebox and again following a 1hr exposure to ambient conditions. In-situ Raman heating experiments were conducted on the same flakes in the same system. For both the air-stability and temperature dependent measurements the Raman spectra were collected using a commercial WiTec Raman microscope. The system consists of 100 X objective lens and a fiber

coupled 532 nm laser which was set to $300\mu\text{W}$, with spectrometer integration times of 300 seconds. For the heating experiments, a custom heater stage consisting of a small aluminum block, cartridge heater, and thermocouple was used to heat the samples up to 600 K. To ensure adequate temperature stability the sample was left at each temperature range for 30 minutes before the next spectra were collected.

STM imaging: TaCo₂Te₂ samples were cleaved using Kapton tape at room temperature inside an ultra-high vacuum (UHV) chamber with a base pressure of $p \approx 2 \times 10^{-10}$ mbar. After cleaving, the samples were directly transferred into the STM head and cooled down to 4.2 K within 2 hours. STM measurements were conducted using a homebuilt STM instrument under cryogenic ($4\text{K} \leq T \leq 24\text{K}$) and UHV (chamber pressure $\approx 2 \times 10^{-10}$ mbar) conditions using a chemically etched tungsten tip which was prepared on a Cu(111) surface through field emission and controlled indentation, as well as calibrated against the Cu(111) Shockley surface state before each set of measurements. Topographies were recorded using constant current (I) mode. STM topography of TaCo₂Te₂ surface was obtained by using bias voltage (V_b) = -5 mV, $I = 4$ nA.

First-principle electronic and phonon calculations: Density functional theory (DFT) calculations were performed to calculate the electronic band structures of TaCo₂Te₂ using the Vienna Ab initio Simulation Package (VASP) *v5.4.4* using the PBE functional. PAW potentials were chosen based on recommended potentials. We used a plane wave energy cutoff of 600 eV. We used Γ – centered $15 \times 15 \times 5$ and $30 \times 15 \times 5$ k -meshes for the undistorted and RT TaCo₂Te₂ structure, respectively. The atomic positions for the undistorted TaCo₂Te₂ structure were allowed to relax with an energy convergence criterion of 10^{-7} eV. A static calculation was performed on each structure with an energy convergence criterion of 10^{-7} eV. Gaussian smoothing was applied to the density of states (DOS) calculation. DFT calculations were performed to calculate phonon band structures of TaCo₂Te₂ compounds using simulations using the QuantumESPRESSO package and the PBEsol functionals found in the QuantumESPRESSO pseudopotential database^{38,39}. For TaCo₂Te₂, an energy cutoff of 65 Rydberg (Ry), together with a $12 \times 6 \times 3$ k -mesh for the self-consistent field (SCF) calculations. An energy threshold of 10^{-10} Ry was used for the SCF. Density functional perturbation theory calculations were performed using a $2 \times 1 \times 1$ q -mesh and an energy threshold of 10^{-20} Ry to determine phonon spectra.

References

1. Janssen T, Janner A. Aperiodic crystals and superspace concepts. *Acta Crystallographica Section B* **70**, 617-651 (2014).
2. de Wolff PM, Janssen T, Janner A. The superspace groups for incommensurate crystal structures with a one-dimensional modulation. *Acta Crystallographica Section A* **37**, 625-636 (1981).
3. Devarakonda A, *et al.* Evidence of striped electronic phases in a structurally modulated superlattice. *Nature* **631**, 526-530 (2024).
4. Perks NJ, Johnson RD, Martin C, Chapon LC, Radaelli PG. Magneto-orbital helices as a route to coupling magnetism and ferroelectricity in multiferroic CaMn₇O₁₂. *Nat. Commun.* **3**, 1277 (2012).
5. Vasiliev A, Volkova O, Zvereva E, Markina M. Milestones of low-D quantum magnetism. *npj Quantum Materials* **3**, 18 (2018).
6. Pinheiro CB, Abakumov AM. Superspace crystallography: a key to the chemistry and properties. *IUCrJ* **2**, 137-154 (2015).
7. Frenkel D. Order through entropy. *Nat. Mater.* **14**, 9-12 (2015).
8. Frenkel D. Order through disorder: Entropy-driven phase transitions. In: *Complex Fluids* (ed Garrido L). Springer Berlin Heidelberg (1993).
9. Pusey PN, van Megen W. Phase behaviour of concentrated suspensions of nearly hard colloidal spheres. *Nature* **320**, 340-342 (1986).
10. Dussi S, Dijkstra M. Entropy-driven formation of chiral nematic phases by computer simulations. *Nat. Commun.* **7**, 11175 (2016).
11. Escobedo FA. Engineering entropy in soft matter: the bad, the ugly and the good. *Soft Matter* **10**, 8388-8400 (2014).
12. Barry E, Hensel Z, Dogic Z, Shribak M, Oldenbourg R. Entropy-Driven Formation of a Chiral Liquid-Crystalline Phase of Helical Filaments. *Phys. Rev. Lett.* **96**, 018305 (2006).

13. Fraden S, Maret G, Caspar DLD, Meyer RB. Isotropic-nematic phase transition and angular correlations in isotropic suspensions of tobacco mosaic virus. *Phys. Rev. Lett.* **63**, 2068-2071 (1989).
14. Božin ES, *et al.* Entropically Stabilized Local Dipole Formation in Lead Chalcogenides. *Science* **330**, 1660-1663 (2010).
15. Tremel W. TaNi₂Te₂, A Novel Layered Telluride, and TaCo₂Te₂, a Structural Variant with Peierls Distortion. *Angewandte Chemie International Edition in English* **31**, 217-220 (1992).
16. Singha R, *et al.* TaCo₂Te₂: An Air-Stable, High Mobility Van der Waals Material with Probable Magnetic Order. *Adv. Funct. Mater.* **32**, 2108920 (2022).
17. Galvis JA, *et al.* Nanoscale phase-slip domain walls in the charge density wave state of the Weyl semimetal candidate $\{\mathrm{NbTe}\}_{4}$. *Phys. Rev. B* **107**, 045120 (2023).
18. Husremović S, *et al.* Encoding multistate charge order and chirality in endotaxial heterostructures. *Nat. Commun.* **14**, 6031 (2023).
19. Gao S, *et al.* Atomic-scale strain manipulation of a charge density wave. *Proc. Natl. Acad. Sci. U.S.A* **115**, 6986-6990 (2018).
20. Abdel-Hafiez M, *et al.* Pressure-induced reentrant transition in $\{\mathrm{Nb}\}_{3}$ phases: Combined Raman scattering and x-ray diffraction study. *Phys. Rev. B* **99**, 235126 (2019).
21. McWhan DB, Fleming RM, Moncton DE, DiSalvo FJ. Reentrant Lock-in Transition of the Charge-Density Wave in $2\mathrm{H}\text{-Ta}\{\mathrm{Se}\}_{2}$ at High Pressure. *Phys. Rev. Lett.* **45**, 269-272 (1980).
22. Nie L, Tarjus G, Kivelson SA. Quenched disorder and vestigial nematicity in the pseudogap regime of the cuprates. *Proc. Natl. Acad. Sci. U.S.A* **111**, 7980-7985 (2014).
23. Tsen AW, *et al.* Structure and control of charge density waves in two-dimensional 1T-TaS₂. *Proc. Natl. Acad. Sci. U.S.A* **112**, 15054-15059 (2015).
24. Savitzky BH, *et al.* Bending and breaking of stripes in a charge ordered manganite. *Nat. Commun.* **8**, 1883 (2017).

25. Pallikara I, Kayastha P, Skelton JM, Whalley LD. The physical significance of imaginary phonon modes in crystals. *Electronic Structure* **4**, 033002 (2022).
26. Gray MJ, *et al.* A cleanroom in a glovebox. *Review of Scientific Instruments* **91**, (2020).
27. Tian Y, *et al.* Understanding the evolution of anomalous anharmonicity in $\text{Bi}_2\text{Te}_3\text{Se}$. *Phys. Rev. B* **95**, 094104 (2017).
28. Du JS, Bae Y, De Yoreo JJ. Non-classical crystallization in soft and organic materials. *Nat. Rev. Mater.* **9**, 229-248 (2024).
29. Chatterjee U, *et al.* Emergence of coherence in the charge-density wave state of 2H-NbSe₂. *Nat. Commun.* **6**, 6313 (2015).
30. Novello AM, *et al.* Stripe and Short Range Order in the Charge Density Wave of Cu_xTiSe_2 . *Phys. Rev. Lett.* **118**, 017002 (2017).
31. Sung SH, *et al.* Endotaxial stabilization of 2D charge density waves with long-range order. *Nat. Commun.* **15**, 1403 (2024).
32. Sung SH, *et al.* Two-dimensional charge order stabilized in clean polytype heterostructures. *Nat. Commun.* **13**, 413 (2022).
33. Hohenberg PC. Existence of Long-Range Order in One and Two Dimensions. *Phys. Rev.* **158**, 383-386 (1967).
34. Yang S, Chen Y, Jiang C. Strain engineering of two-dimensional materials: Methods, properties, and applications. *InfoMat* **3**, 397-420 (2021).
35. Bianco E, Kourkoutis LF. Atomic-Resolution Cryogenic Scanning Transmission Electron Microscopy for Quantum Materials. *Accounts of Chemical Research* **54**, 3277-3287 (2021).
36. Savage JR, Hopp SF, Ganapathy R, Gerbode SJ, Heuer A, Cohen I. Entropy-driven crystal formation on highly strained substrates. *Proc. Natl. Acad. Sci. U.S.A* **110**, 9301-9304 (2013).

37. Son S, *et al.* Strongly adhesive dry transfer technique for van der Waals heterostructure. *2D Materials* **7**, 041005 (2020).
38. Giannozzi P, *et al.* Advanced capabilities for materials modelling with Quantum ESPRESSO. *J. Phys. Condens. Matter* **29**, 465901 (2017).
39. Giannozzi P, *et al.* QUANTUM ESPRESSO: a modular and open-source software project for quantum simulations of materials. *J. Phys. Condens. Matter* **21**, 395502 (2009).

Acknowledgements

This project is supported by the Gordon and Betty Moore Foundation's EPIQS initiative through award number GBMF9064 (supported L.M.S. and N.M., R.S., S.C., and F.Y.), the Princeton Center for Complex Materials (PCCM) and the NSF-MRSEC program (supports. L.M.S. and F.Y.) (MRSEC; DMR-2011750) and the Air Force Office of Scientific Research under Grants No. FA9550-24-1-0110 (supports L.M.S., K.S.B., R.S., and V.M.P.). N.M., F.Y., G.C., N.Y., and L.M.S. acknowledge the sample characterization of the Imaging and Analysis Center (IAC) at Princeton University, partially supported by the Princeton Center for Complex Materials (PCCM) and the NSF-MRSEC program (MRSEC; DMR-2011750). B.J. acknowledges support by the Hong Kong RGC (C6033-22G) and the Croucher Foundation (Grant No. CIA22SC02). C.C. acknowledges support from the Tin Ka Ping Foundation. S.B.L. and G.C. are supported by the National Science Foundation Graduate Research Fellowship Program under Grant No. DGE-2039656. Any opinions, findings, and conclusions or recommendations expressed in this material are those of the author(s) and do not necessarily reflect the views of the National Science Foundation. I.E. acknowledges funding from the Spanish Ministry of Science and Innovation (Grant No. PID2022-142861NA-I00) and the Department of Education, Universities and Research of the Basque Government and the University of the Basque Country (Grant No. IT1527-22). M.G.V. received financial support from the Canada Excellence Research Chairs Program for Topological Quantum Matter. M.G.V. and F.B. thank support to the Spanish Ministerio de Ciencia e Innovacion grant PID2022-142008NB-I00 and the Ministry for Digital Transformation and of Civil Service of the Spanish Government through the QUANTUM ENIA project call - Quantum Spain project, and by the European Union through the Recovery, Transformation and Resilience Plan - NextGenerationEU within the framework of the Digital Spain 2026 Agenda. This project was

partially supported by the European Research Council (ERC) under the European Union's Horizon 2020 Research and Innovation Programme (Grant Agreement No. 101020833).

Author contributions

N.M. and L.M.S. founded the idea of the project. N.M. and R.S. synthesized the compound. N.M. designed and conducted the exfoliation/nanoflake transfer process. N.M. and G.C. prepared TEM samples and conducted TEM experiments and analysis. G.C. and F.Y. prepared FIB cut samples. J.C. and C.C. performed STM measurements. B.J. provided insights on and supervised the STM measurements. F.B. performed phonon calculations with the help and insight of I.E. and M.G.V. G.C. performed electronic band structure calculations. V.M.P. carried out Raman measurements with supervision and insight from K.S.B. S.B.L. performed the single crystal X-Ray measurements and data analysis. S.C. helped in reorganization of the main text in the manuscript. All data were analyzed by N.M. with L.M.S. supervising. N.M. and L.M.S. wrote the first draft of the manuscript. All authors provided discussion of results and scientific input to the manuscript.

Competing interests: The authors declare that they have no competing interests.

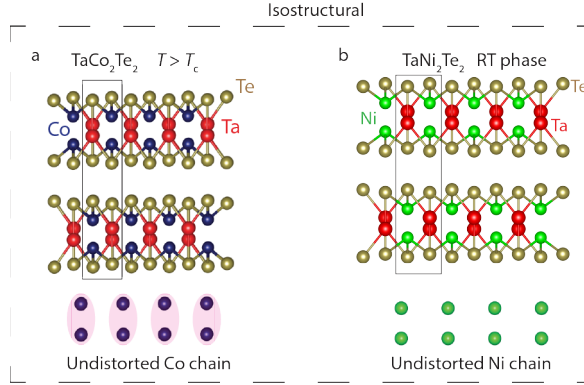
Supplementary Information for

Emergence of reentrant structural modulations far beyond the thermal limit

Nitish Mathur¹, Guangming Cheng², Francesc Ballester^{3,4}, Gabrielle Carrel¹, Vincent M. Plisson⁵, Fang Yuan¹, Jiangchang Zheng⁶, Caiyun Chen⁶, Scott B. Lee¹, Ratnadwip Singha^{1,7}, Sudipta Chatterjee¹, Kenneth S. Burch⁵, Berthold Jäck⁶, Ion Errea^{3,4,8}, Maia G. Vergniory^{3,9}, Nan Yao², Leslie M. Schoop^{1*}

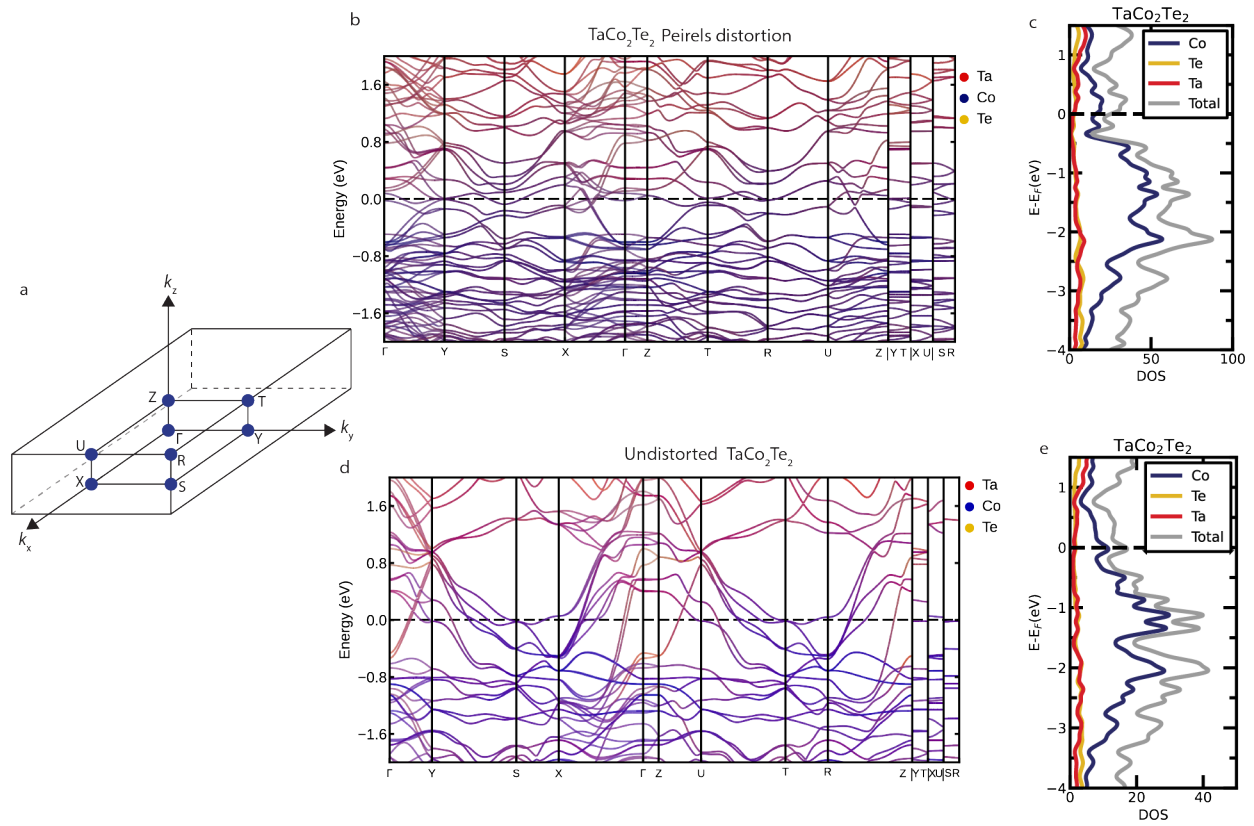
1. Department of Chemistry, Princeton University, Princeton, NJ 08544, USA.
2. Princeton Materials Institute, Princeton, NJ 08544, USA.
3. Donostia International Physics Center, 20018 Donostia-San Sebastián, Spain.
4. Department of Applied Physics, University of the Basque Country (UPV/EHU), 20018 Donostia-San Sebastián, Spain.
5. Department of Physics, Boston College, Chestnut Hill, MA USA.
6. Department of Physics, The Hong Kong University of Science and Technology, Clear Water Bay, Kowloon, Hong Kong SAR.
7. Department of Physics, Indian Institute of Technology Guwahati, Assam 781039, India.
8. Centro de Física de Materiales (CSIC-UPV/EHU), 20018 Donostia-San Sebastian, Spain.
9. Département de Physique et Institut Quantique, Université de Sherbrooke, Sherbrooke, J1K 2R1 Québec, Canada.

Corresponding author* email: lschoop@princeton.edu

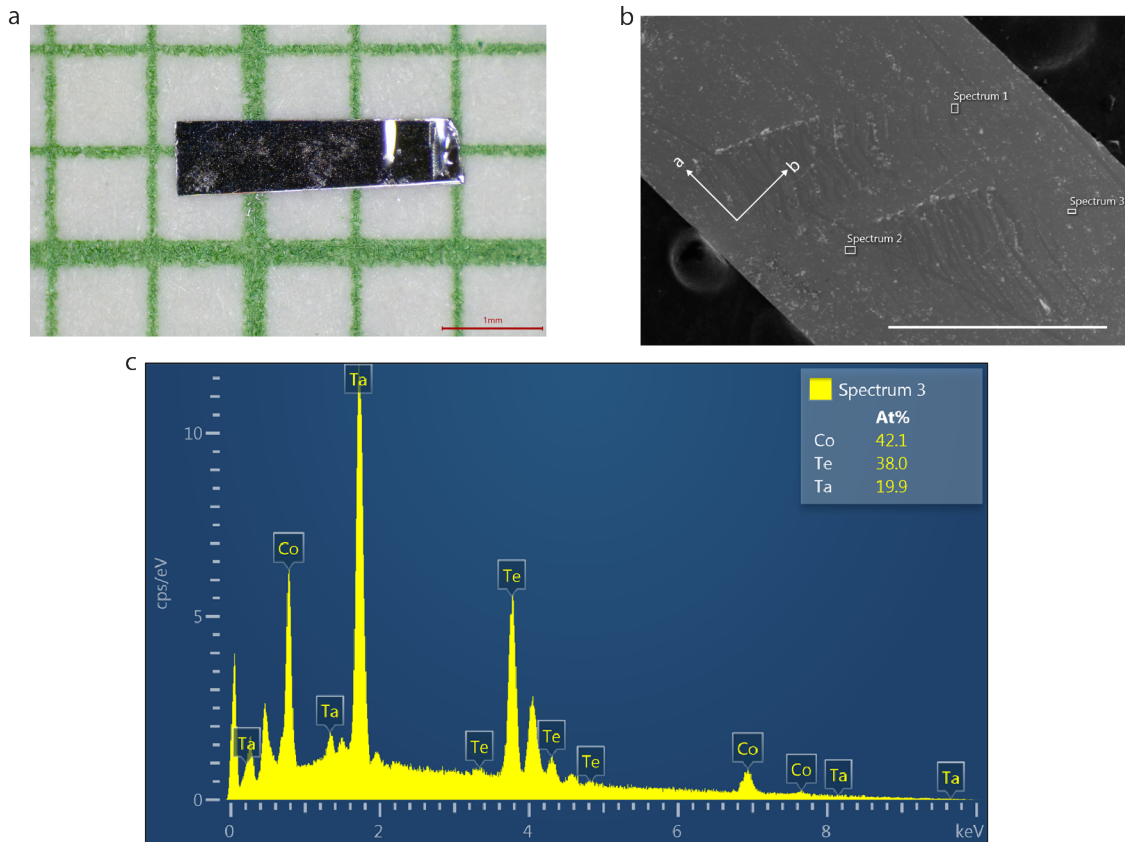


Supplementary Fig. 1: Crystal structural of undistorted TaCo_2Te_2 and TaNi_2Te_2 . (a) Schematic of the undistorted TaCo_2Te_2 , stable above the critical temperature (T_c) is isostructural with (b) the room-temperature (RT) structure of TaNi_2Te_2 , which features undistorted Ni chains.

Supplementary Note 1. The crystallographic information file for the undistorted TaCo_2Te_2 structure ($a = 0.3304$ nm, $b = 0.6579$ nm, $c = 1.7781$ nm) above T_c was derived from the standard unit cell of the isostructural RT orthorhombic TaNi_2Te_2 ($a = 0.3566$ nm, $b = 0.6488$ nm, $c = 1.7014$ nm). To obtain the undistorted structure, the lattice parameters were first adjusted to match the distorted standard unit cell of TaCo_2Te_2 ($a = 0.6608$ nm, $b = 0.6579$ nm, $c = 1.7781$ nm) along the b - and c -axes, followed by halving the unit cell along the a -axis. Both structures share the same space group ($Pnma$, no. 62), as reported in ref. 15 of the main text.



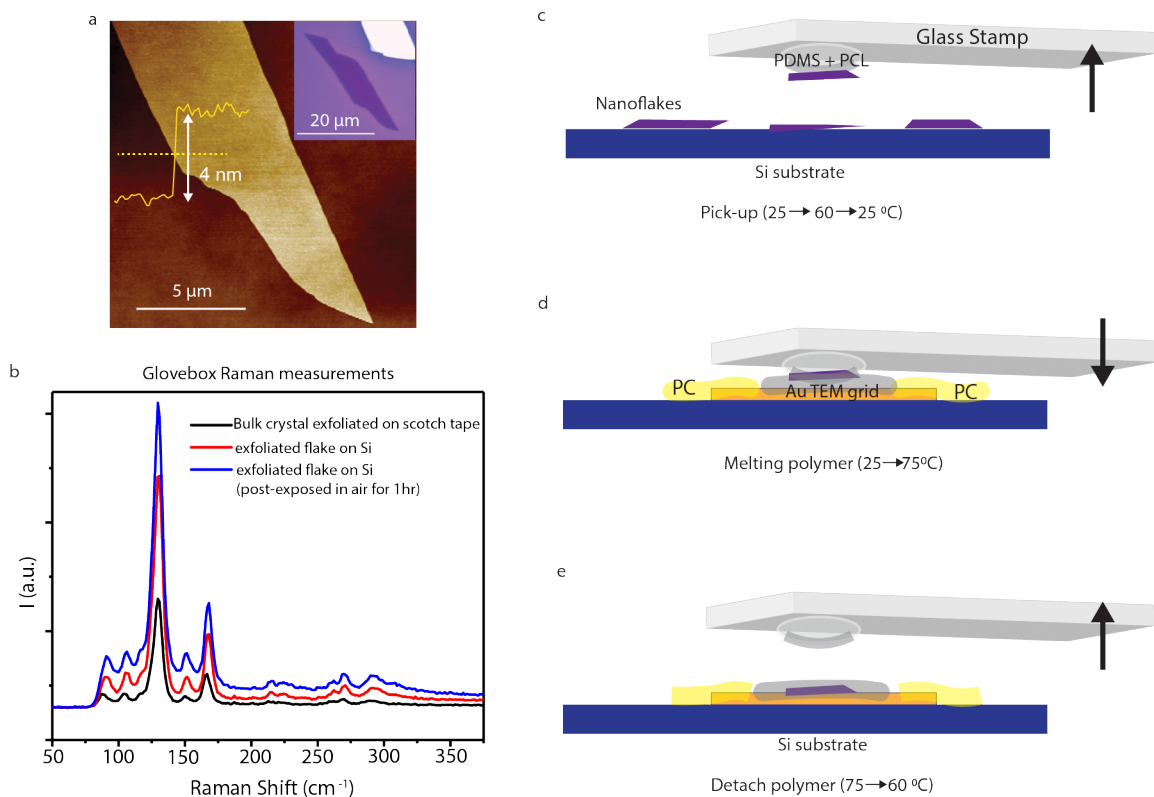
Supplementary Fig. 2: Calculated electronic band-structures of TaCo₂Te₂ : (a) 3D Brillouin zone of the TaCo₂Te₂ structure used for first principle calculations. (b) Electronic band-structure of Peierls distorted TaCo₂Te₂ with (c) corresponding density of states (DOS) over a large energy range (d) Electronic band-structure of undistorted TaCo₂Te₂ with (e) corresponding DOS over a large energy range. Both structures show metallic bands near Fermi energy.



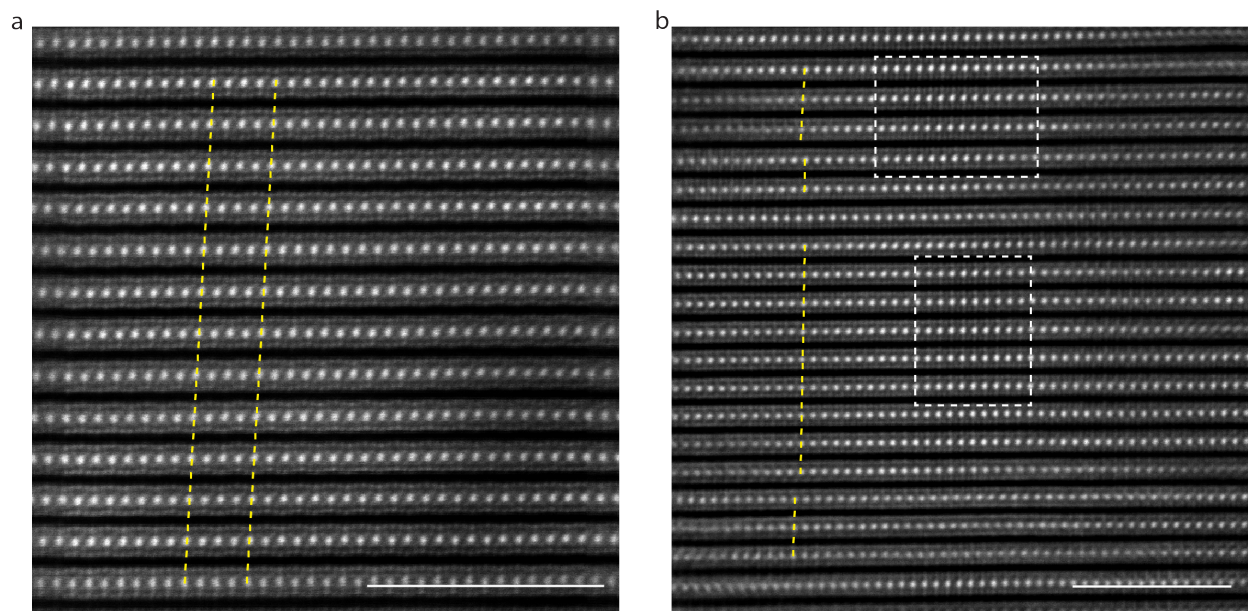
Supplementary Fig. 3: Oriented TaCo_2Te_2 crystals synthesized *via* chemical vapor transport. **(a)** Optical microscope image of a millimeter-sized TaCo_2Te_2 crystal. **(b)** SEM image of the crystal used for FIB cut TEM samples. **(c)** Representative SEM-EDS spectrum of the analysis area demonstrating the presence of Ta, Co, and Te elements. Scale bar in panel b is 0.5 mm.

Supplementary Table 1: Compositional analysis of a TaCo_2Te_2 single crystal. The atomic % of each element determined from 3 regions of the TaCo_2Te_2 single crystal shown in Supplementary Fig. 3b.

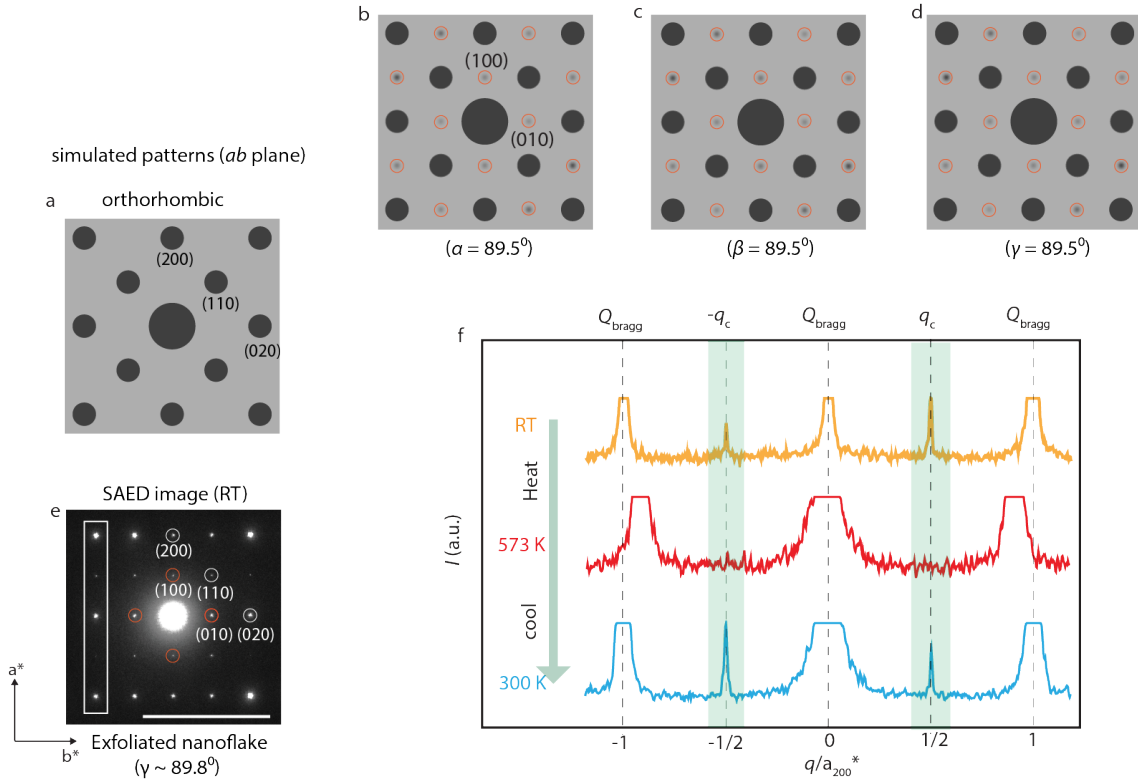
Spectrum	Atomic % Ta	Atomic % Co	Atomic % Te	Ratio (Ta: Co: Te)
1	19.4	43.2	37.5	1: 2.21 : 1.93
2	19.4	42.4	38.0	1: 2.18 : 1.95
3	19.9	42.1	38.0	1: 2.11 : 1.90



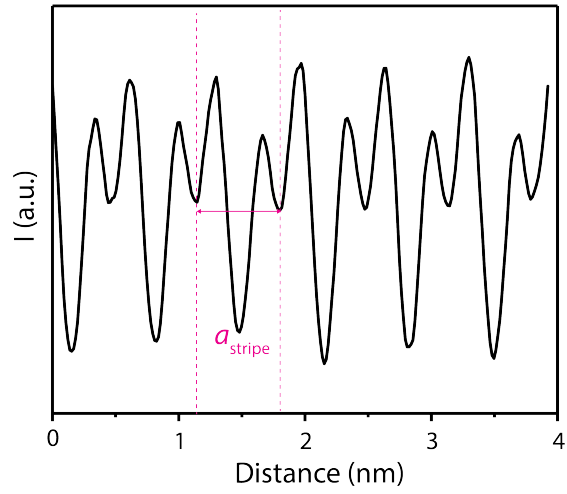
Supplementary Fig. 4: Exfoliation, air-stability, and polymer-transfer method of TaCo₂Te₂ exfoliated nanoflakes. (a) AFM image of a TaCo₂Te₂ thin flake (thickness \approx 4 nm). Inset showing the optical microscope image of the nanoflake on a Si/SiO₂ (285 nm) substrate. (b) Glovebox Raman spectroscopy demonstrates the air stability of exfoliated nanoflakes. Raman spectra show no new peaks even after 1 hour of air-exposure following glovebox exfoliation. (c-e) Schematics illustrating the complete pick-up and transfer process of TaCo₂Te₂ nanoflakes onto a Au TEM grid using PCL/PDMS glass stamps. PC was used to secure the thin TEM grid to the Si substrate due to its higher glass transition temperature than PCL. These diagrams also indicate the temperature ranges applied at each step of the process.



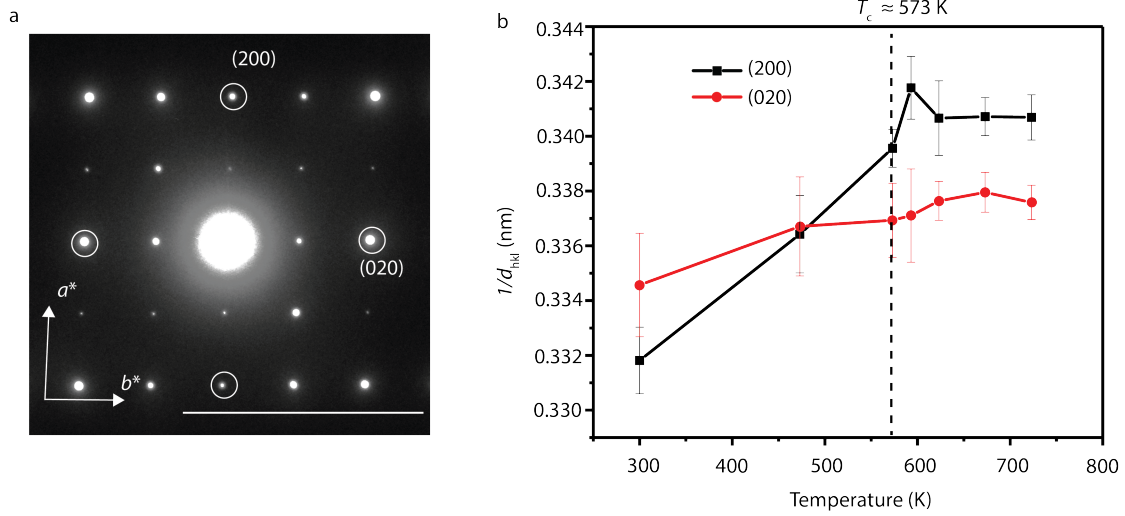
Supplementary Fig. 5: Processed high-resolution cross-sectional HAADF-STEM images of distorted and undistorted TaCo₂Te₂ structure collected at (a) RT and (b) 673 K, respectively. These are larger area STEM images shown in Fig.1c,d in the main text. Some areas lack clarity in showing the undistorted structure, marked by dashed white boxes in panel b, possibly due to thermal drift. The dashed yellow line in panel b highlights interlayer slips and stacking faults, which are not evident in the RT image shown in panel a. Scale bar in panels a,b is 5 nm.



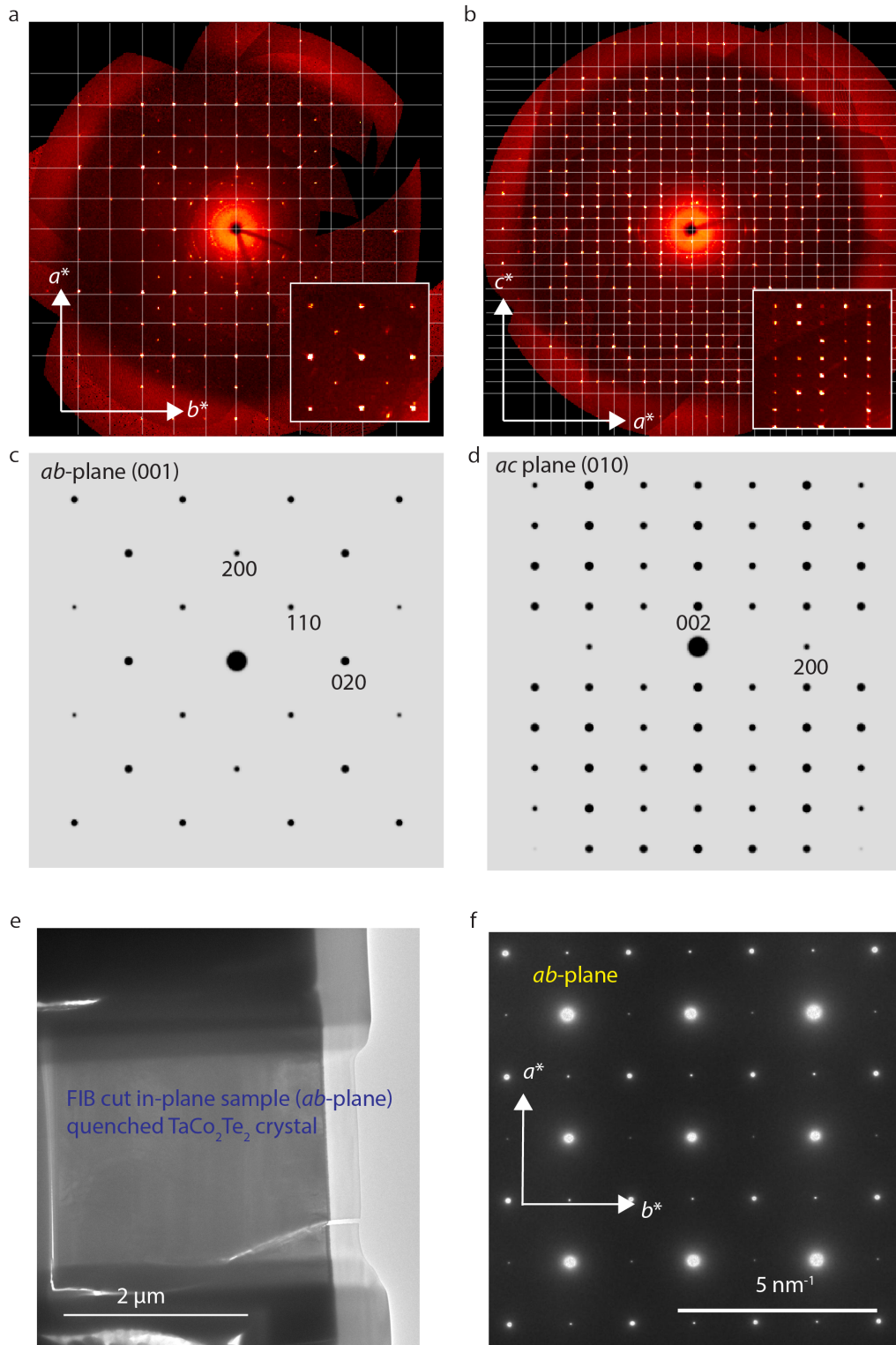
Supplementary Fig. 6: Forbidden reflections and reversible structural phase transition shown via TEM diffraction of TaCo_2Te_2 nanoflakes. (a) The simulated ab -plane TEM diffraction of orthorhombic distorted TaCo_2Te_2 (b-d) Simulated ab -plane TEM diffractions revealing weak forbidden reflections resulting from a monoclinic distortion between any lattice vectors. (e) SAED image of a TaCo_2Te_2 nanoflake with both Bragg and forbidden reflections marked with white and red circles, respectively. (f) Reversible structural phase transition determined by temperature evolution of Bragg and superlattice peaks intensities along a^* direction, marked with dashed box in panels e. This reveal structural modulation with wavevector $q_c \approx a_{200}^*/2$.



Supplementary Fig. 7: Intensity line-cut to determine the real space modulation (a_{stripe}) of the stripe-like pattern shown in Fig. 1j in the main text.



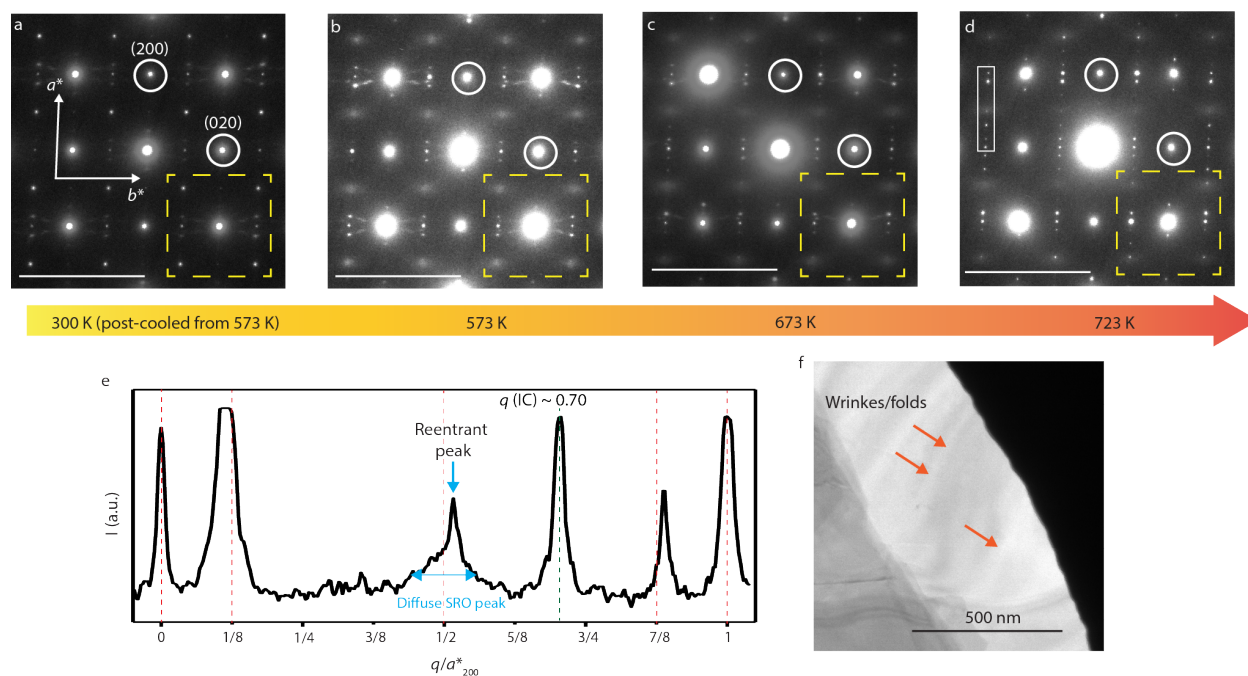
Supplementary Fig. 8: Temperature induced lattice-expansion of TaCo_2Te_2 determined from SAED images of the ab -plane (a) A family of crystallographic planes (200) and (020) of the undistorted unit cell along a and b lattice vectors, marked with white circles. (b) The temperature dependent interplanar distance of the (200) and (020) planes. The slope of lattice expansion along the distortion axis, i.e. a -axis, is steeper compared to the b -axis, with a sharp decrease in the slope above T_c .



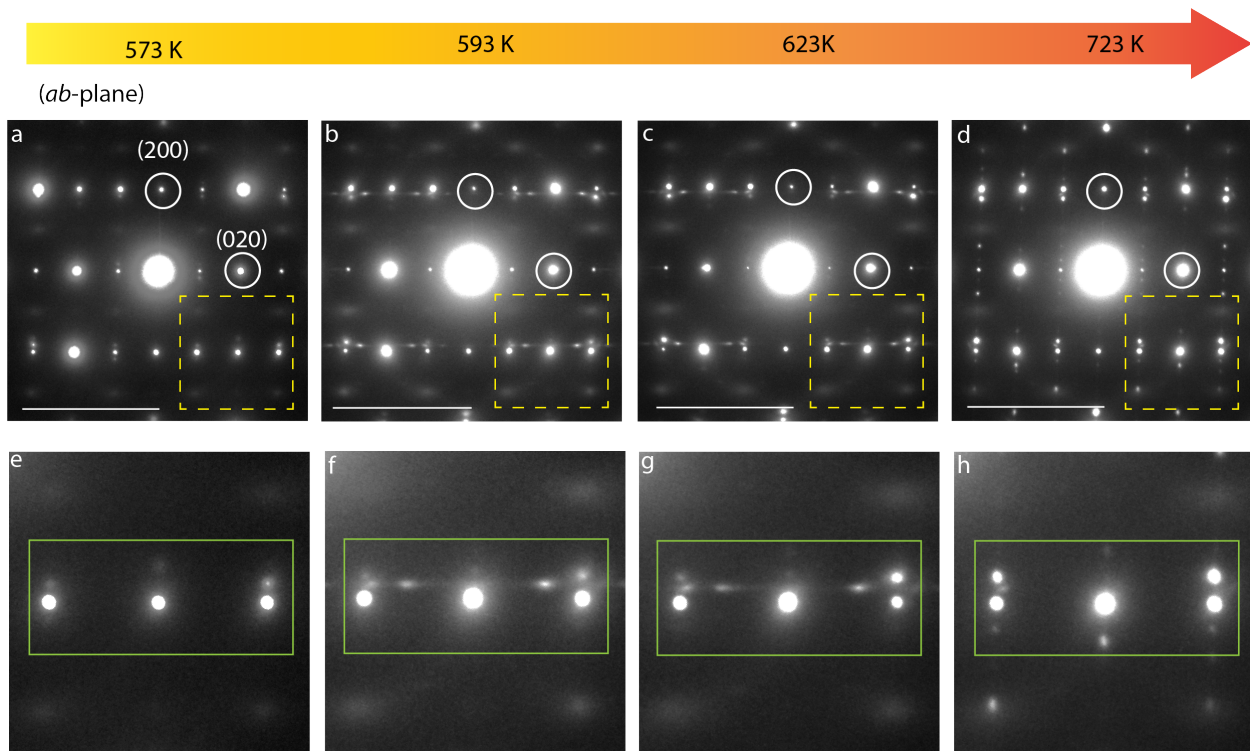
Supplementary Fig. 9: Structural analysis of TaCo_2Te_2 crystals quenched at 773K. Reconstructed precession images from single-crystal X-ray diffraction along ab and ac plane. Overlaid reciprocal lattice grids (white lines) are shown for the orthorhombic unit-cell. Simulated diffraction patterns of (c) ab and (d) ac planes matched with precession images shown in panel a,b. (e) Bright-field image of a FIB cut in-plane (ab -plane) TEM sample. (f) Corresponding SAED image of the ab -plane collected at RT matches with the RT TaCo_2Te_2 structure.

Supplementary Table 2 : Minor peak deviation of commensurate ($q_n = q/2n$) wave-vectors, reentrant peaks, and incommensurate (q (IC)) wave-vectors in SAED images of TaCo₂Te₂ nanoflakes and FIB cut samples shown in the main text.

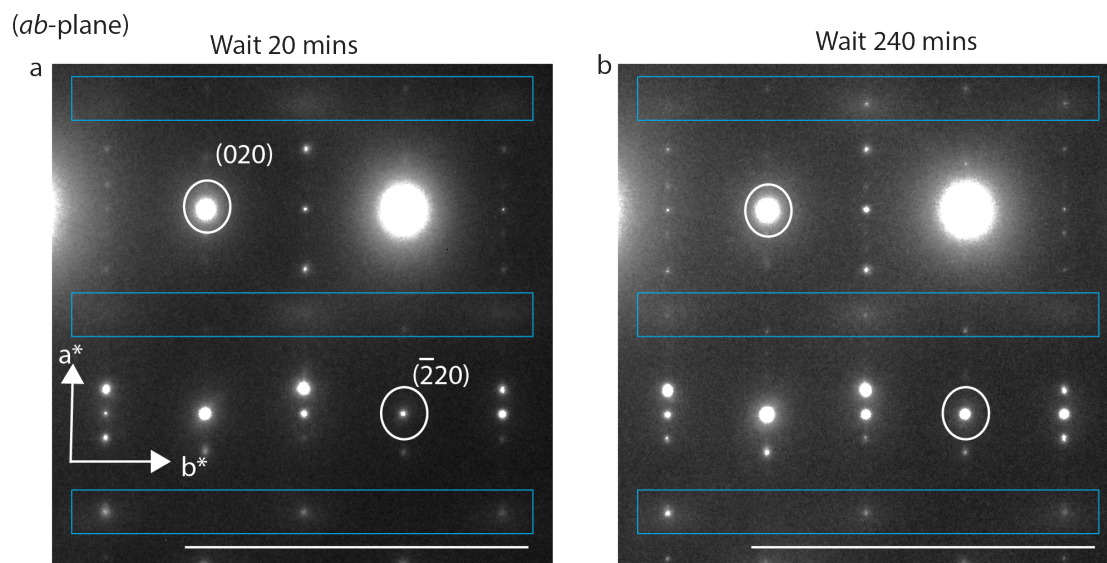
Nanoflakes (723 K)	q_2 (dev.)	q_4 (dev.)	$1-q_2$ (dev.)	$1-q_4$ (dev.)	Reentrant peak (dev.)	q (IC)
Flake 2 ($h30$), Fig.2	-	0.1255 (0.0005)	-	0.884 (0.009)	-	0.706
Flake 2 ($h40$), Fig.2	0.248 (- 0.002)	-	0.754(0.004)			0.412
Flake 3 ($h-30$), Fig.4	-	0.113(-0.012)	-	0.888(0.013)	0.515 (0.015)	0.706
FIB lamella- ab -plane ($h10$), Fig.3	-	0.118 (-0.007)	-	0.893(0.018)	0.507 (0.007)	0.706



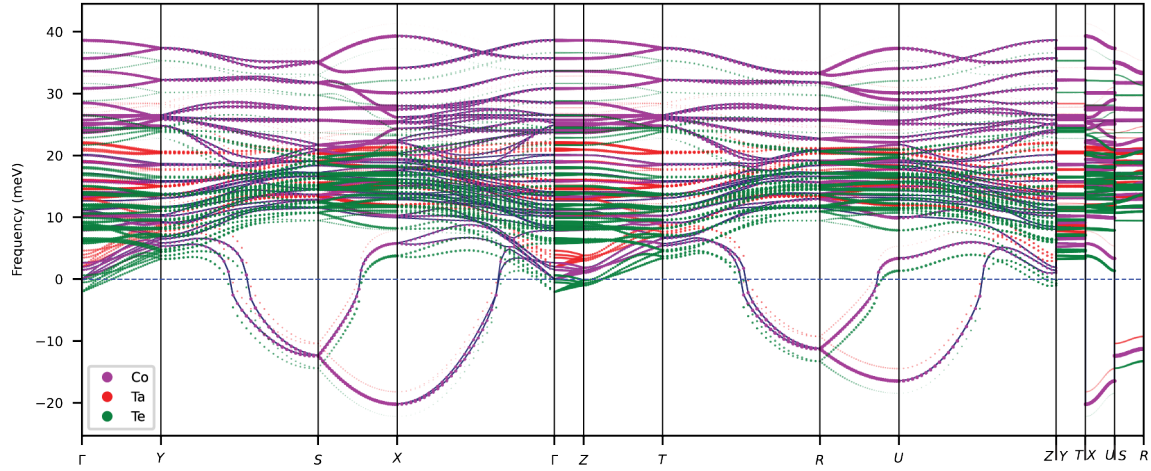
Supplementary Fig. 10: In-situ heating TEM diffraction of an exfoliated TaCo₂Te₂ nanoflake (Flake 3). **(a-d)** SAED images of a TaCo₂Te₂ nanoflake from Fig. 4 in the main text. Yellow dashed boxes highlight the zoomed area images in the main text **(e)** Representative intensity line scans of SAED peaks marked with a white box along the a^* direction in panels d. **(f)** Bright Field image of the nanoflake with mesoscopic defects marked with red arrows. Scale bar in panels a-d is 5 nm⁻¹.



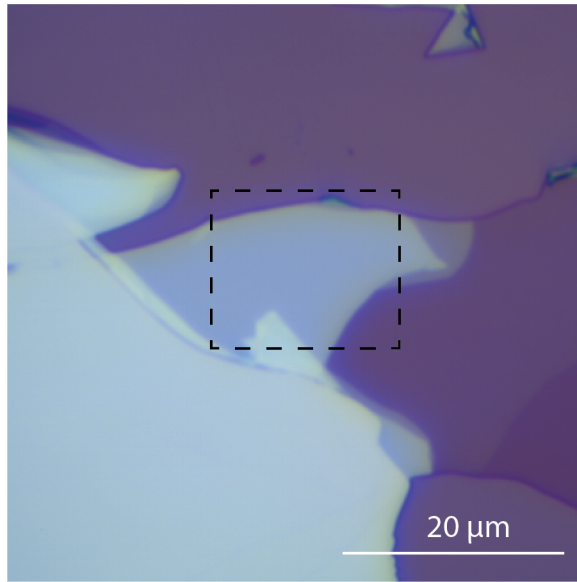
Supplementary Fig. 11: Temperature evolution of weakly coherent phases above T_c : (a-d) SAED images of the *ab*-plane of a TaCo₂Te₂ exfoliated nanoflake (Flake 2). (e-h) Corresponding zoomed images of areas marked by yellow dashed boxes in panels (a-d). As temperature increases above T_c , the weakly coherent ordered peaks gradually disappear and long-range modulations increases along the a^* direction, observed as increasing intensities of superlattice peaks. Scale bar in panels a-d is 5 nm^{-1} .



Supplementary Fig. 12: Time-dependent emergence of the reentrant primary order at 723 K. (a) SAED images of the *ab*-plane of a TaCo₂Te₂ exfoliated nanoflake (Flake 4) collected after waiting for (a) 20 mins and (b) 240 mins at 723 K. Blue boxes in both images highlight peaks from the reentrant phase.



Supplementary Fig. 13: Phonon band calculations of the undistorted TaCo₂Te₂ with projections from each element. Phonon bands of each element are offset for clarity. Bands of all elements contribute to dynamic structural instabilities in the undistorted TaCo₂Te₂.



Supplementary Fig. 14: Optical microscope image of exfoliated TaCo₂Te₂ nanoflakes on a Si substrate. The one outlined with a dashed black box used for in-situ heating Raman measurements.